Applied Catalysis B: Environmental 326 (2023) 122185

Contents lists available at ScienceDirect

Applied Catalysis B: Environmental

journal homepage: www.elsevier.com/locate/apcatb

Enhancing CO_2 electroreduction to syngas by active protons of imidazolium ionic liquids: From performance to mechanism

Zhaojun Min [a], Bing Chang [b], Chunfeng Shao [a], Xiaofang Su [a], Nan Wang [a], Zhiyong Li [a], Huiyong Wang [a], Yang Zhao [a], Maohong Fan [c,*], Jianji Wang [a,*]

[a] Key Laboratory of Green Chemical Media and Reactions (Ministry of Education), Collaborative Innovation Center of Henan Province for Green Manufacturing of Fine Chemicals, School of Chemistry and Chemical Engineering, Henan Normal University, Xinxiang, Henan 453007, PR China
[b] Key Laboratory for Yellow River and Huai River Water Environment and Pollution Control (Ministry of Education), School of Environment, Henan Normal University, Xinxiang, Henan 453007, PR China
[c] College of Engineering and Applied Science, and School of Energy Resources, University of Wyoming, Laramie, WY 82071, USA

ARTICLE INFO

Keywords:
CO_2 reduction reaction
Syngas
Active protons
Ionic liquid
Nano-Ag@Ni foam

ABSTRACT

High current density at specific CO/H_2 molar ratios is the key to the industrial application of heterogeneous electrocatalytic CO_2 reduction reaction (CO_2RR) to syngas, which is still very challenging. Here, we report a Ni-foam-supported nano-Ag catalyst for CO_2RR in ionic liquid (IL)-acetonitrile electrolyte originally designed for CO_2RR-to-CO. It is surprising to find that this is a highly efficient catalytic system for CO_2RR-to-syngas, the CO/H_2 molar ratio in the syngas can be tuned from 1:5–26:1, and the current density is as high as 363.6, 458.2, and 644.7 mA cm^{-2} at the CO/H_2 molar ratios of 1:1, 1:2, and 1:3, respectively. The high efficiency of CO_2RR-to-syngas is attributed to the synergistic stabilization action of nano-Ag and IL cationic C4/5-H for intermediate $*COO^-$ to produce CO, as well as cationic C2-H contribution to hydrogen evolution. This work opens a new way to improve catalytic performance of CO_2RR-to-syngas.

1. Introduction

Carbon dioxide (CO_2) is the main greenhouse gas, and its excessive emission has brought a series of environmental concerns [1,2]. Meanwhile, CO_2 is also an important intermediate carrier of energy transmission [3]. Electrocatalytic CO_2 reduction reaction (CO_2RR) to value-added chemicals and fuels is attractive for renewable energy storage and mitigation of the environmental problem [4–6]. As a basic raw feedstock for many industrial products, syngas can be used for different purposes based on the molar ratio of CO to H_2 [7,8]. Typically, the hydroformylation process holds the optimal CO/H_2 molar ratio of 1:1. In contrast, Fischer-Tropsch synthesis requires a wider range of molar ratios, such as 1:2 for methanol and dimethyl ether, 1:3 for methane, 2:3 for acetaldehyde, and 2:5 for ethylene productions [9]. It is believed that CO_2RR-to-syngas is the most desirable route to realize industrial applications of CO_2 first [10].

Electrochemical CO_2RR-to-syngas mainly depend on the design of catalysts that control the molar ratio of CO/H_2 and enhance current density according to needs [11]. For this purpose, many catalysts have been designed for electrochemical CO_2RR-to-syngas with tunable CO/H_2 molar ratios, including porous Au nanostructures, [12] Ag/C_3N_4, [13] alloy, [14,15] metal oxides/sulfides, [16–18] and single-atom catalysts [19,20]. Although an increasing number of catalysts have been reported for electrocatalytic CO_2RR-to-syngas and considerable achievements have been made in recent years, [21,22] the current density at a specific CO/H_2 molar ratio is far from the requirements of industrial application [23].

Besides the catalysts, electrolyte plays a significant role in tuning the molar ratio range of CO/H_2 and improving the current density at a specific molar ratio in CO_2RR [24]. Ionic liquids (ILs), as functionalized organic molten salts at low temperatures, have been widely used in CO_2 capture and electrochemical conversion due to their wide electrochemical windows, high CO_2 solubility, and structure-designable characteristic [3,25–27]. Many studies have shown that ILs can significantly reduce overpotential and stabilize reaction intermediates, [28–30] so they have been used to tune CO/H_2 molar ratio range and increase the current density for CO_2RR-to-syngas [31–34]. For example, by using 1-ethyl-3-methylimidazolium triflate ($[C_2mim][OTf]$) electrolyte, the CO/H_2 molar ratio could be tuned from 1:1–4:1, and the current density was 17 mA cm^{-2} at the molar ratio of 1:1 [32,33]. In contrast, in

* Corresponding authors.
E-mail addresses: mfan@uwyo.edu (M. Fan), jwang@htu.edu.cn (J. Wang).

https://doi.org/10.1016/j.apcatb.2022.122185
Received 25 July 2022; Received in revised form 25 October 2022; Accepted 13 November 2022
Available online 19 November 2022

1-butyl-3-methylimidazolium hexafluorophosphate ([C_4mim][PF_6]) electrolyte, the molar ratio of CO/H_2 would be regulated from 1:3–24:1. The current density was increased to 90 mA cm^{-2} at the molar ratio of 1:1 in H-cell, [34] which is significant progress. However, the current density is still low for industrial applications, and understanding the involved mechanism of ILs is also a significant challenge.

Herein, we developed a nano-Ag catalyst in-situ grown on Ni foam (nano-Ag@Ni foam) for CO_2RR in [C_4mim][PF_6]/acetonitrile (MeCN) electrolyte without water in the cathode chamber originally designed for CO production. Unexpectedly, we found that this is a highly efficient electrocatalytic system for CO_2RR-to-syngas, the CO/H_2 molar ratio in the syngas could be tuned from 1:5–26:1 by controlling the reduction potential, and the current density in a flow cell was high up to 644.7 mA cm^{-2}, which is comparable to the record created in the electrochemical CO_2RR-to-syngas by using dual single-cobalt atom electrocatalysts.[22] Furthermore, by methylating the imidazolium cationic C2-H, we could switch the CO_2RR product from syngas to just CO over a wide range of reduction potential, and the corresponding current density was as high as 528.3 mA cm^{-2}. In a systematic mechanism study, the intermediates *COOH and *CO on the nano-Ag catalyst were identified by in situ Raman spectroscopy; proton tracer and quantum chemical calculations revealed that in the IL-MeCN electrolyte, C2-H of the imidazolium cation ([C_4mim]$^+$) was mainly responsible for H_2 evolution, while its C4/5-H stabilized radical intermediate *COO^- for CO generation. Thus, the synergistic effect of the IL in electrolyte and the nano-Ag catalyst is the key to the remarkable performance observed for the electrocatalytic CO_2RR-to-syngas.

2. Experimental methods

2.1. Preparation of nano-Ag@Ni foam catalyst

A piece of Ni foam with the thickness of 0.5 mm was cut into 2 × 2 cm^2 and treated with acetone and 1.0 M HCl (each for 30 min), respectively. The Ni foam was then washed with absolute alcohol and deionized water under sonication and dried in a vacuum oven at 50 ℃ for 2 h. Then, 3.0 mmol $AgNO_3$ and 0.4567 g thiourea were dissolved in 60 mL of ethylene glycol, and the solution was transferred into a 100 mL Teflon reactor to impregnate the dried Ni foam. The reactor was heated to 100 ℃ at a rate of 2 ℃ min^{-1} and then kept for 6 h. After cooling to room temperature, the sample was washed with deionized water and dried with ethanol to obtain the nano-Ag@Ni foam catalyst material. Material characterization see supporting information.

2.2. Electrochemical CO_2 reduction measurements in H-cell

Electrochemical measurements in an H-cell were performed by an electrochemical station (CHI660E). A 0.25 × 1 cm^2 nano-Ag@Ni foam with a thickness of 0.5 mm functioned as a working electrode, while Ag/Ag^+ (0.01 M $AgNO_3$ and 0.1 M tetrabutylammonium perchlorate in MeCN solution) electrode and Pt mesh served as the reference and counter electrode, respectively. All potentials were standardized to ferrocene/ferrocenium (Fc/Fc^+), and the details of potential conversion and reference electrode calibration were provided in supporting information. The electrolyte of the anode compartment of the H-cell was 0.1 M aqueous H_2SO_4 solution, while that of the cathode compartment was 30 wt% [C_4mim][PF_6] in MeCN (Fig. S1). Prior to the electrochemical tests, CO_2 was purged into the electrolyte for 30 min with a flow rate of 30 mL min^{-1} to remove the residual air in the reservoir. LSV and CV tests were performed in CO_2-saturated 30 wt% [C_4mim][PF_6]/MeCN electrolyte with a scan rate of 50 mV/s. Faradaic efficiency of CO and H_2 was determined by using Eq. (1):

$$FE_{(CO\ \ or\ \ H_2)} = \frac{n_{(CO\ \ or\ \ H_2)} F C_{(CO\ \ or\ \ H_2)} V}{Q} \quad (1)$$

where n is the number of charge transfers (n = 2), F is the Faraday constant (96,485.34 C mol^{-1}), C is the concentration of H_2 or CO obtained from the GC (mol L^{-1}), V is the volume of CO_2 consumed during electrolysis (L), Q is the total electricity during this process, which could be obtained from the electrochemical working station directly or integration of the i-t curve. Here, the electrode area used to calculate the current density was 2 times the projected area of 0.25 × 1 cm^2 nano-Ag@Ni foam electrode, and the current density obtained was the geometric density.

2.3. H/D exchange experiment

H/D exchange measurements were conducted in the same H-cell described above for the electrochemical CO_2 reduction measurements. The electrolyte of its anode and cathode compartments was 0.1 M D_2SO_4-D_2O and 30 wt% [C_4mim][PF_6]/MeCN, respectively, and the cathode and anode chambers were isolated by proton exchange membrane. In this way, the interference caused by adding D_2O directly to the cathode pool could be avoided, and the movement track of D proton might be observed more clearly. To saturate the electrolyte with different gases, the electrolyte was purged for at least 30 min with Ar (99.999 vol%) or CO_2 (99.999 vol%). ^{2}H NMR spectra of the electrolyte were determined at different reduction potentials in Ar and CO_2 atmosphere.

2.4. In-situ Raman spectroscopy

The CO_2RR on nano-Ag@Ni foam cathode was performed in an in situ Raman electrolysis H-cell (Wuhan Gaoshi Ruilian Technology Co., Ltd) filled with CO_2-saturated 30 wt% [C_4mim][PF_6]/MeCN electrolyte. In situ Raman spectra were measured by a laser confocal high-resolution Raman spectrometer (Villeneuve d'Ascq, France). The excitation laser wavelength was 532 nm, and the power was about 5 mW. A 50 × long working distance objective and a 90° adaptor were used. Each Raman spectrum displayed here was recorded with six accumulations over an acquisition time of 20 s

2.5. Isotope labeling

^{13}C isotope labeling measurements were performed in the H-cell described above. First, a gas collecting bag was filled with $^{13}CO_2$, and a peristaltic pump was used to circulate the $^{13}CO_2$ gas between the cathode electrolyte and the gas collecting bag to make sure the electrolyte was saturated with $^{13}CO_2$. Then the gas-phase products produced by electrochemical reduction of CO_2 at − 2.17 V (vs. Fc/Fc^+) were then collected. Finally, gas chromatography-mass spectrometry was used to determine the gas species and their composition in the gas bag, from which the carbon source of the product produced in the CO_2RR process could be identified.

3. Results and discussion

3.1. Structural features of the catalytic material

Ag and Ni are abundant metals on earth. Ag is often reported to be an efficient catalyst for selective electroreduction of CO_2 to CO, while Ni foam has a large surface area and good electrical conductivity [35–38]. Thus, nano-Ag supported on Ni foam (nano-Ag@Ni foam) was chosen as the electrocatalyst in the present work. The nano-Ag catalyst in-situ grown on Ni foam was synthesized by a solvothermal approach. X-ray diffraction (XRD) patterns of the nano-Ag@Ni foam and neat Ni foam were illustrated in Fig. 1**a**. The peaks at 38.12°, 44.28°, 64.43°, and 77.47° could be assigned to the Ag plane of (111), (200), (220), and (311), which coincide with the XRD characteristic peaks of pure silver (PDF No. 04–0783). The peaks at 31.94°, 51.69°, and 56.78° reflect the (002), (112), and (202) crystal planes of Ni_2O_3 (PDF No.14–0481),

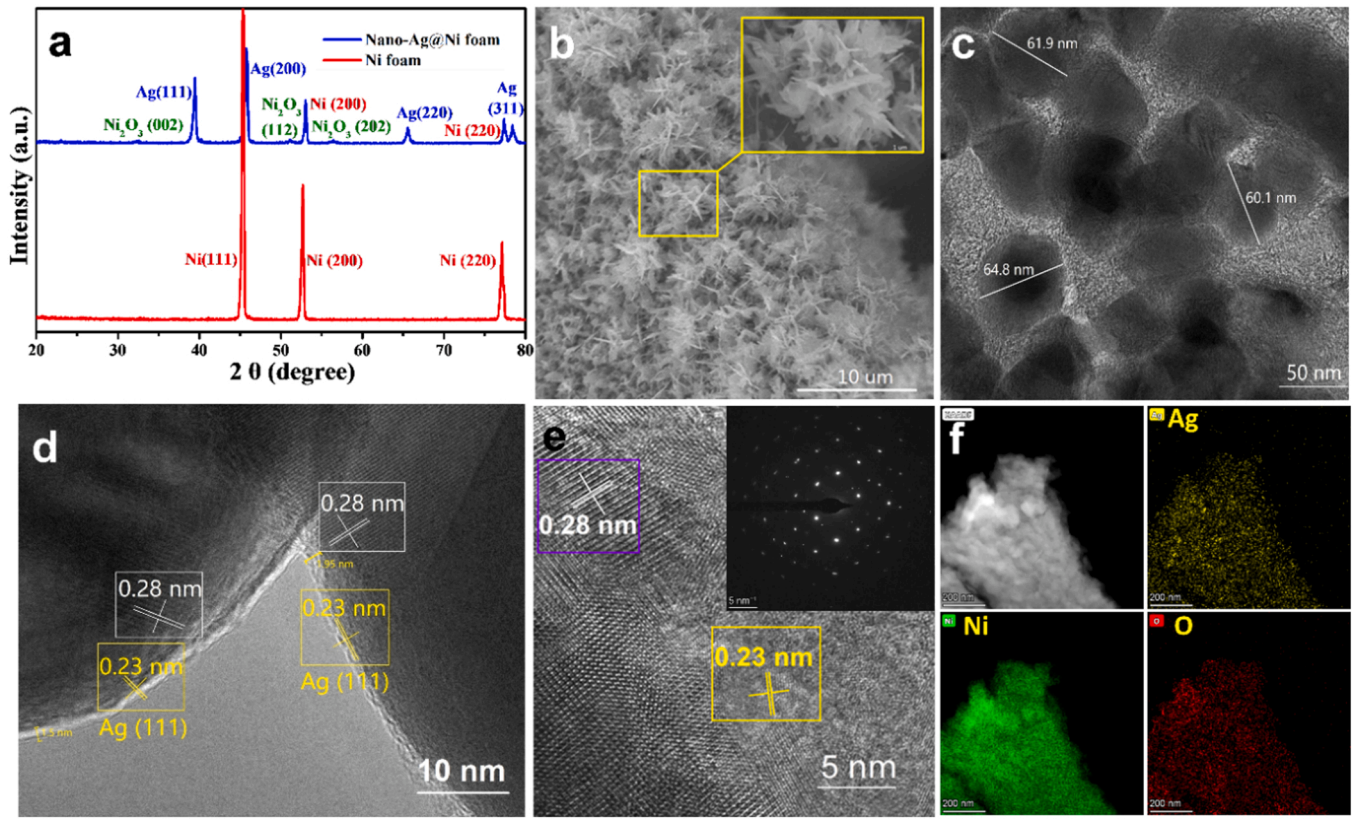

Fig. 1. Composition and structure of nano-Ag@Ni foam. (a) XRD, (b) SEM, (c)TEM, (d) and (e) high-resolution TEM (HR-TEM) images, and (f) EDS elemental mapping analysis.

respectively. The remaining peaks are ascribed to the Ni foam substrate, which matches well with the PDF card of Ni foam (PDF No. 04–0850).

From scanning electron microscopy (SEM) image of the nano-Ag@Ni foam, it is clear that the catalyst exhibited a 3D flower morphology formed by stacking nanosheets (Fig. 1**b** and **S2**). Transmission electron microscope (TEM) images (Fig. 1**c** and **S3**) of the nano-Ag@Ni foam show that the nanosheets were composed of small particles with particle sizes between 50 and 220 nm. The high-resolution TEM (HR-TEM) images indicate that the lattice fringe spacing of the small particles was 0.28 nm, which belongs to the (002) crystal plane of Ni_2O_3 [39]. The lattice fringe spacing at the edge of the small particles was 0.23 nm, which corresponds to the Ag (111) crystal plane (Fig. 1**d**, **e,** and **S4**). Furthermore, from the HR-TEM image (Fig. 1**d**) of the nanosheet cross-section, the thickness of the outer layer silver was about 1.5–2.5 nm. Elemental distributions showed that the nano-Ag@Ni foam catalyst was composed of Ag, Ni, and O elements (Fig. 1**f**), and the Ag almost covered the whole surface of the nano-Ag@Ni foam. These results suggest that the small particles were Ni_2O_3 coated with Ag.

X-ray photoelectron spectroscopy (XPS) of the nano-Ag@Ni foam illustrates the typical peaks of Ag 3*d*, Ni 2*p,* and O 1 *s* (Fig. 2). As shown in Fig. 2**b**, the Ag 3*d* peaks of nano-Ag@Ni foam were located at 367.9 and 373.9 eV, and the spin-orbital separation of the two peaks was about 6 eV, which corresponds to the characteristic peak of zero-valent silver, indicating that Ni foam was loaded with Ag^0 [40]. The Ni 2*p* spectrum (Fig. 2**c**) exhibited two main peaks at 855.4 and 872.9 eV together with two satellite peaks at 861.4 and 879.5 eV, which are assigned to Ni $2p_{3/2}$ and Ni $2p_{1/2}$ of Ni^{2+}, while the Ni 2*p* peaks at 856.8 and 874.5 eV are ascribed to Ni $2p_{3/2}$ and Ni $2p_{1/2}$ of Ni^{3+}, respectively. These results demonstrate that Ni on the surface of the nano-Ag@Ni foam catalyst was oxidized into Ni^{2+} and Ni^{3+} [41–43]. The XPS spectrum of O 1 *s* (Fig. 2**d**) could be resolved into two peaks, in which the peak located at 531.2 eV corresponds to the metal-oxygen bond of Ni_2O_3, [44] and the peak centered at 532.2 eV may be identified as the O atoms in the adsorbed water molecules [45,46]. From the above analysis, we can confirm that the catalytic material prepared here was Ni_2O_3 nanosheets covered with Ag^0 and supported by Ni foam.

3.2. Electrocatalytic performance of CO_2RR to syngas

The catalytic activity of nano-Ag@Ni foam for CO_2RR was first investigated in an H-cell (Fig. S1) with IL in MeCN electrolytes without water in the cathode chamber. Under such circumstances, the possible reactions at the anode and cathode can be expressed by the following equations:

$$\text{Anode: } 2H_2O \rightarrow O_2(g) + 4H^+ + 4e^- \quad (2)$$

$$\text{Cathode: } CO_2 + 2\,H^+ + 2e^- \rightarrow CO(g) + H_2O \quad (3)$$

$$2H^+ + 2e^- \rightarrow H_2(g) \quad (4)$$

Here, imidazolium ILs with different anions $[PF_6]^-$ and $[BF_4]^-$ were selected. To investigate the cationic structure effect, 1-alkyl-3-methylimidazolium hexafluorophosphate ($[C_nmim][PF_6]$, n = 2, 4, 6, 8, 10) and tributyl (tetradecyl) phosphonium hexafluorophosphate ($[P_{44414}][PF_6]$) were examined. The CO_2RR products in IL/MeCN electrolytes and Faradaic efficiency (FE) of the products were shown in Table S1. It can be seen that among the electrolytes investigated in this work, the FE of CO (FE_{CO}) product was the highest in $[C_4mim][PF_6]$/MeCN electrolyte. With increasing $[C_4mim][PF_6]$ content in MeCN, the FE_{CO} values significantly increased initially and then reached the maximum at 30 wt % of $[C_4mim][PF_6]$ (Fig. 3**a**). Although the highest current density was observed at 40 wt% of $[C_4mim][PF_6]$ (Fig. 3**b**), the FE_{CO} at this composition was not optimal. Thus, 30 wt% of $[C_4mim][PF_6]$ in MeCN was chosen as the optimal electrolyte for the electrochemical CO_2RR-to-syngas.

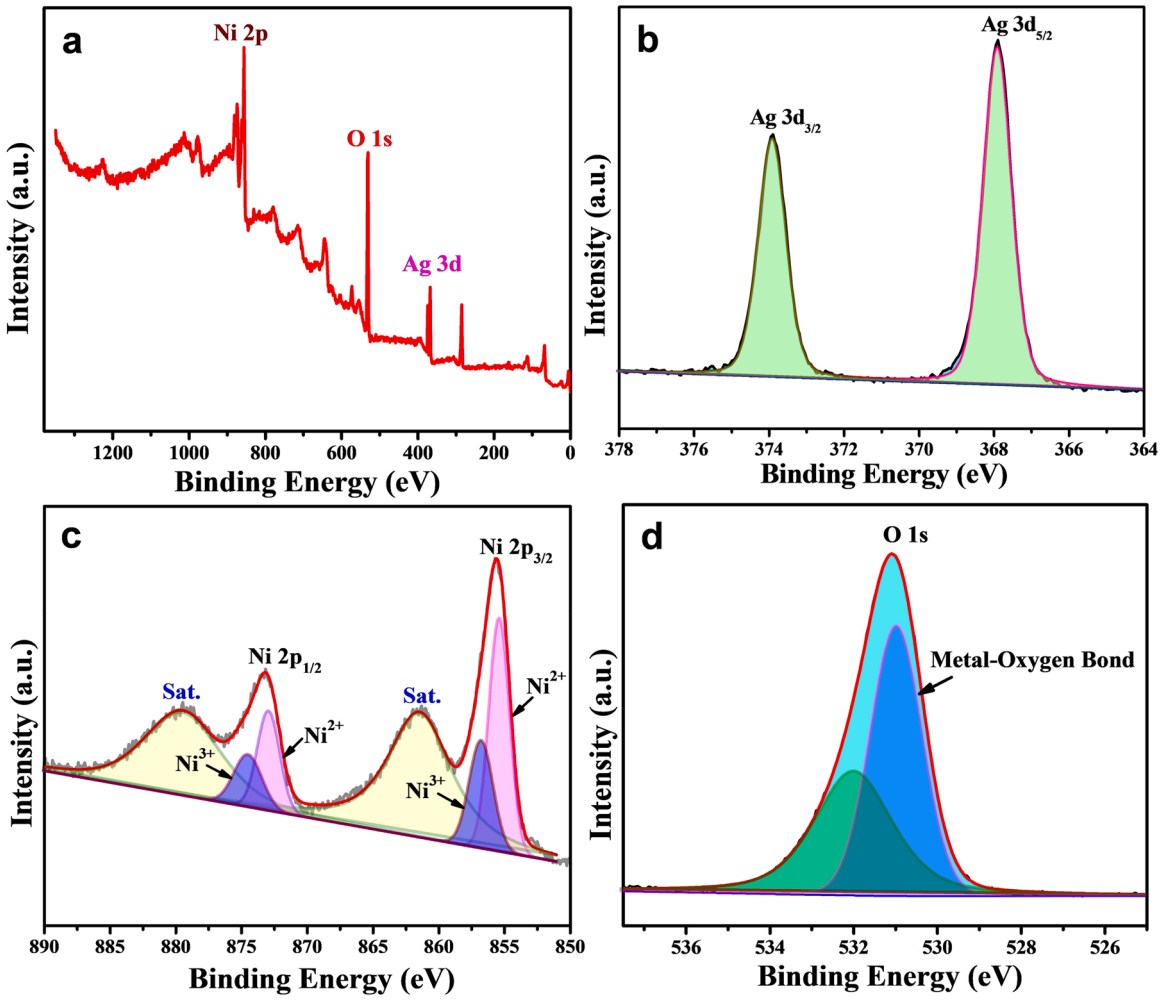

Fig. 2. XPS spectra of the nano-Ag@Ni foam catalyst. (a) XPS survey spectra, (b) Ag 3*d*, (c) Ni 2*p*, and (d) O 1 *s* XPS.

The linear sweep voltammetry (LSV) curves of Ni foam and nano-Ag@Ni foam in Ar/CO_2-saturated [C_4mim][PF_6]/MeCN electrolyte were given in Fig. 3**c**. In the potential range of − 2.77 ~ − 1.57 V (vs. Fc/Fc^+), the nano-Ag@Ni foam had a higher current density than Ni foam in the Ar-saturated electrolyte. Since the possible reduction reactions are H_2 evolution reaction (HER) and electrolyte reduction in this case, this result suggests that the nano-Ag@Ni foam was conducive to HER and electrochemical reduction of the electrolyte. However, in the CO_2-saturated system, the current density over nano-Ag@Ni foam electrode was significantly increased compared with that in the Ar-saturated system (Fig. 3**c**), illustrating that electrochemical reduction of CO_2 occurred on the nano-Ag@Ni foam electrode [34]. It is also noted from the LSV and i-t curves (Figs. S5 and S6) that the nano-Ag@Ni foam had a higher current density than both Ni foam and neat Ag at the same potential, and the FE_{CO} reached 96.1% at − 2.17 V (vs. Fc/Fc^+), confirming the remarkable catalytic effect of nano-Ag on the Ni foam for CO_2RR-to-CO. On the other hand, neat Ag and nano-Ag@Ni foam exhibited high and similar FE_{CO}, but low FE_{CO} was observed for Ni foam (Fig. S6, and Table S2), which indicates that Ag was the main element for the catalysis of CO_2RR-to-CO. Furthermore, the electrochemically active surface areas (ECSAs) of the three catalysts were determined by measuring double-layer capacitance (Cdl, see the CV curves in Fig. S7–9) [47]. From the results shown in Fig. 3**d**, the nano-Ag@Ni foam was found to have the largest ECSA value (8.18 mF cm^{-2}), which was roughly 7.4 and 4.9 times that of Ag (1.11 mF cm^{-2}) and Ni foam (1.68 mF cm^{-2}), respectively. This result showed that the electrochemical reduction activity of the catalyst significantly increased when the nano-Ag was in-situ grown on Ni foam.

Fig. 4**a** shows the FE values of the CO_2RR products at different reduction potentials in [C_4mim][PF_6]/MeCN electrolyte. It is clear that at − 1.97 V (vs. Fc/Fc^+), there was only H_2 in the product, suggesting that the reduction potential was not sufficient to activate CO_2 for its electroreduction to CO. As the potential decreased, the FE_{CO} rapidly increased and then decreased, while the opposite trend was observed for FE_{H2}. At − 2.17 V (vs. Fc/Fc^+), the maximum FE_{CO} of 96.1% appeared, and the corresponding molar ratio of CO to H_2 in the product was 26:1. When the potential was reduced to − 2.32 V (vs. Fc/Fc^+), the molar ratio of CO/H_2 was 1:1, and the current density was 122.7 mA cm^{-2} in the H-cell. As the potential was further decreased to − 2.37 and − 2.47 V (vs. Fc/Fc^+), the CO/H_2 molar ratio in the product was close to 1:2 and 1:3, and the current density was 142.3 and 196.9 mA cm^{-2} in the H-cell (Fig. S10), respectively. The nano-Ag@Ni foam in [C_4mim][PF_6]/MeCN electrolyte could effectively catalyze the electrochemical CO_2RR-to-syngas, and the molar ratio range of CO/H_2 was greatly expanded. On the other hand, the current density at a specific CO/H_2 ratio was also significantly improved, which is comparable with the current record reported recently (Table S4) by using dual single-cobalt atom electrocatalysts [22]. Remarkably, from the result of 10 h electrolytic stability tests shown in Fig. 4**b**, the current density at − 2.17, − 2.32, and − 2.47 V (vs. Fc/Fc^+) was stable at 48.2, 122.7, and 196.9 mA cm^{-2}, respectively, and the FE_{CO} values were kept almost unchanged, indicating that the nano-Ag@Ni foam had good stability in the process of CO_2RR-to-syngas.

Interestingly, when [C_4mim][PF_6] was replaced by 1,2-dimethyl-3-

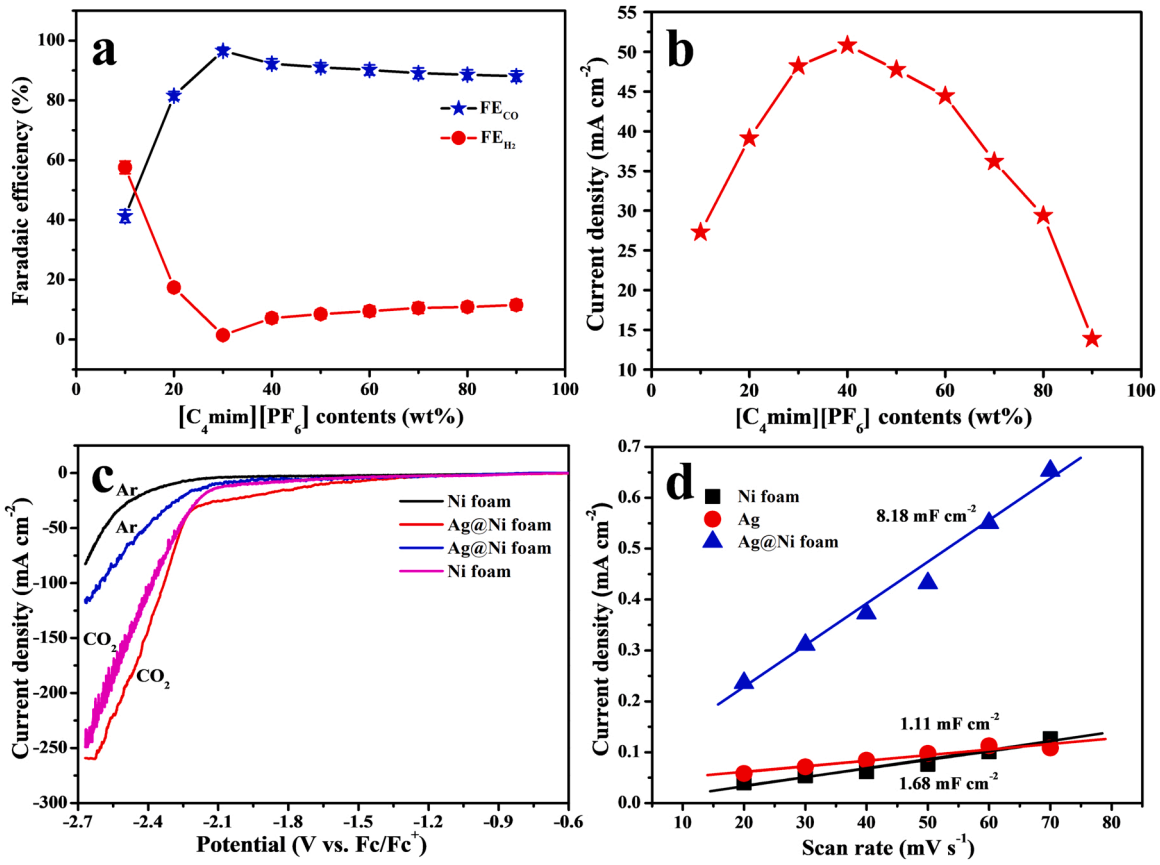

Fig. 3. Electrochemical characterization of the catalyst in Ar/CO_2-saturated [C_4mim][PF_6]/MeCN electrolyte. (a) FE_{CO} at − 2.17 V (vs. Fc/Fc^+) as a function of IL content in the electrolyte, (b) total current density of CO_2RR at − 2.17 V (vs. Fc/Fc^+) as a function of IL content in the electrolyte, (c) LSV curves of Ni foam and nano-Ag@Ni foam catalysts, and (d) the electrochemically active surface area.

butylimidazolium hexafluorophosphate ([C_4mmim][PF_6]) in the electrolyte, where cationic C2-H of the imidazolium IL was replaced by methyl, the FE_{CO} was close to 100% (almost no H_2 in the product) over a wide potential range, and the current density was high up to 168.6 mA cm^{-2} at − 2.47 V (vs. Fc/Fc^+, Fig. 4**c**, Fig. S11 and Table S3). Therefore, the CO_2RR product could be switched between syngas and CO by substituting C2-H of [C_4mim]$^+$. Moreover, at least 10 h stability of CO_2RR-to-CO with a FE_{CO} above 92% was observed in [C_4mmim][PF_6]/MeCN electrolyte (Fig. 4**d**). To examine the carbon source of the CO_2RR products, an isotope labeling experiment using $^{13}CO_2$ as the reactant was performed. The results indicate that the carbon source of CO_2RR products was CO_2 rather than MeCN and IL in the electrolyte (Fig. S12 and S13).

Furthermore, the catalytic performance of nano-Ag@Ni foam for CO_2RR-to-syngas was also investigated in a flow cell (see details in Supporting Information). It is interesting to find that in [C_4mim][PF_6]/MeCN electrolyte, the current density was as high as 363.6, 458.2, and 644.7 mA cm^{-2} at the CO/H_2 molar ratio of 1:1, 1:2, and 1:3, respectively (Fig. S14). After cationic C2-H of the imidazolium IL was replaced by methyl, the current density of the CO_2RR-to-CO was up to 528.3 mA cm^{-2} (Fig. S15). Thus, the nano-Ag@Ni foam was a highly efficient catalyst for CO_2RR-to-syngas and CO_2RR-to-CO in IL electrolyte, such high current densities are very encouraging for industrial application.

3.3. *The possible mechanism for electrocatalytic CO_2RR to syngas*

To study the reaction process of CO_2 on nano-Ag@Ni foam catalyst in IL electrolyte, in situ Raman, ^1H and ^2H NMR, and FT-IR spectra were determined at different potentials. First, we acquired in situ Raman spectra in 30 wt% [C_4mim][PF_6]/MeCN electrolyte, and the result was shown in Fig. 5 and S16. It is noted that a new peak appeared at 473 cm^{-1} for the nano-Ag@Ni foam catalyst (Fig. S16), which could be assigned to Ag-CO stretching vibration [48]. The peaks at 1110 cm^{-1} (Fig. 5**a**) and 1561 cm^{-1} (Fig. 5**b**) belong to the symmetrical and antisymmetrical stretching of *COO^- derived from *COOH [49]. Furthermore, the peak at 2043 cm^{-1} (Fig. 5**c**) in Raman spectra was assigned to CO stretching of the adsorbed *CO on the nano-Ag@Ni foam [50]. Thus, CO_2 was adsorbed on the nano-Ag@Ni foam electrode, followed by its hydrogenation and consecutive formations of *COOH, *CO, and CO, and then desorption of CO. In addition, the intensity of all the above peaks showed a decreasing trend at low potentials, indicating the decline of intermediate production and thus CO_2 reduction to CO under low potential. This is consistent with the result that HER is the primary reaction under low potentials observed experimentally. Similarly, in-situ Raman spectroscopy confirmed that the reaction intermediates were also *COOH (at 1561 cm^{-1}) and *CO (at 2043 cm^{-1}, Fig. S17) for the CO_2RR happened in [C_4mmim][PF_6]/MeCN electrolyte.

To reveal the role of active protons of the ILs in the CO_2RR process, a **H/D** exchange experiment was performed in H-cell (Fig. 6**a**), and the carbon atom numbering (C2-H, C4-H, and C5-H) was given in Fig. 6**b**. It was found that without electrolysis, the C2-H and C4/5-H of [C_4mim][PF_6] were stable and no **H/D** exchange was observed, regardless of the presence or absence of CO_2 (Fig. S18 and S19). However, the situation was quite different under electrolysis. At − 1.97 ~ − 2.17 V (vs. Fc/Fc^+), the imidazolium cationic C2-H at 9.15 ppm was replaced by C2-D at 8.73 ppm, while C4/5-H at 7.51–7.63 ppm was kept unchanged in the Ar atmosphere; at the potential of − 2.37 ~ − 2.57 V (vs. Fc/Fc^+), **H/D** exchange occurred in both C2-H and C4/5-H (Fig. S20) and H_2 was detected as the only electrochemical reduction product under the same

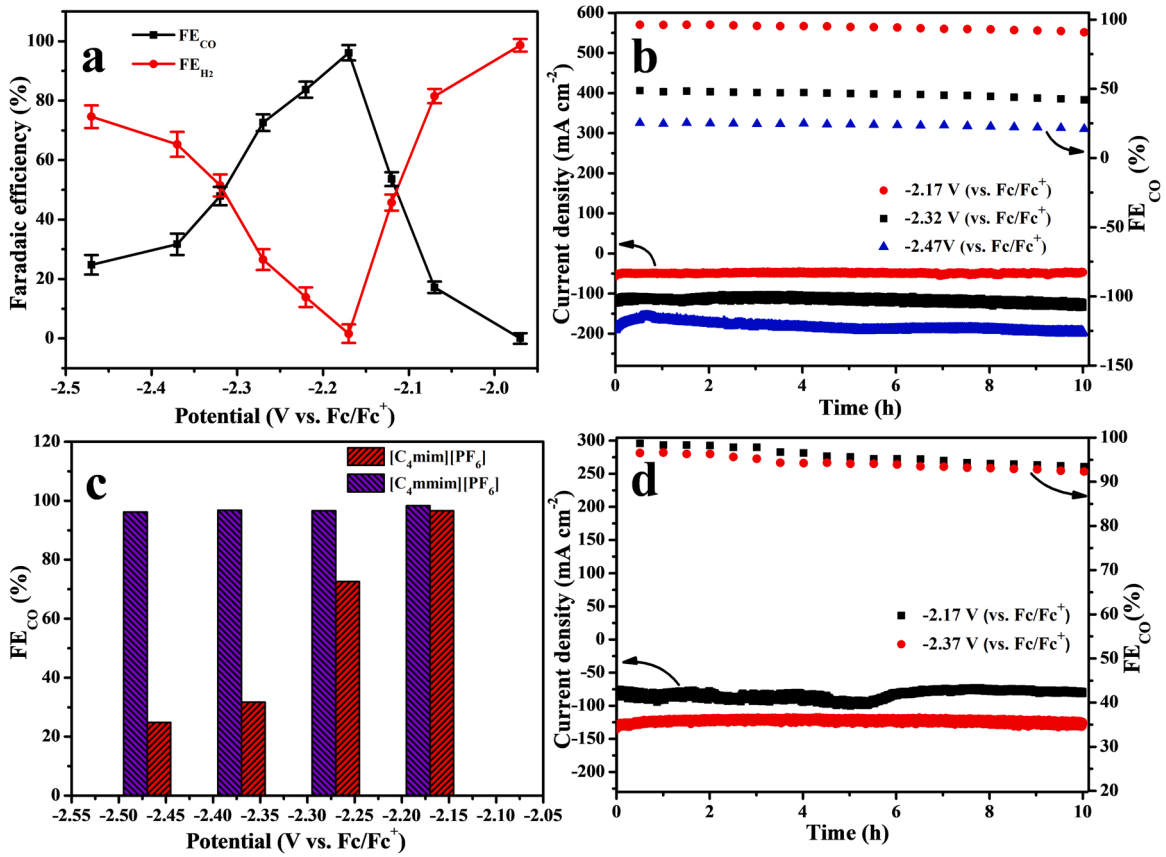

Fig. 4. (a) FE_{CO} and FE_{H2} values at various potentials in $[C_4mim][PF_6]$/MeCN electrolyte, (b) Electrochemical stability of nano-Ag@Ni foam in $[C_4mim][PF_6]$/MeCN electrolyte, (c) The FE_{CO} values at various potentials in $[C_4mim][PF_6]$/MeCN and $[C_4mmim][PF_6]$/MeCN electrolytes, (d) Electrochemical stability of nano-Ag@Ni foam in $[C_4mmim][PF_6]$/MeCN electrolyte.

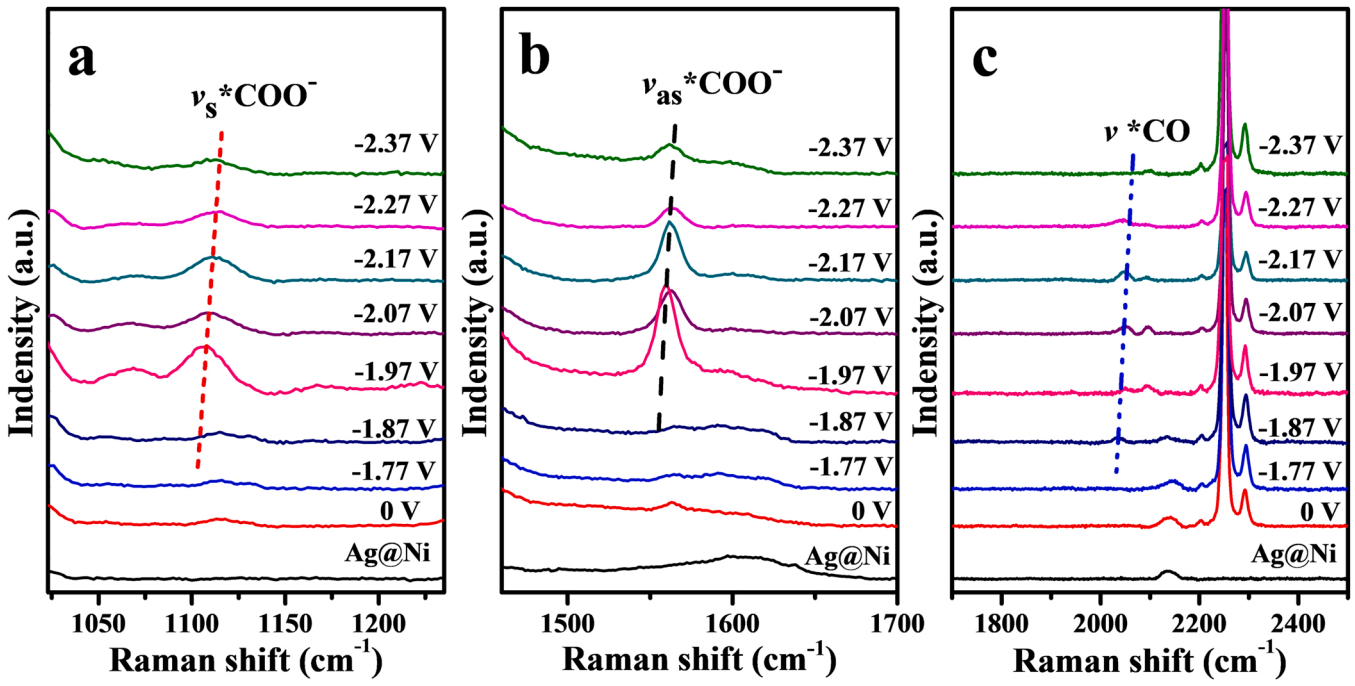

Fig. 5. The in situ Raman spectrum of CO_2RR in $[C_4mim][PF_6]$/MeCN electrolyte at different potentials (vs. Fc/Fc^+).

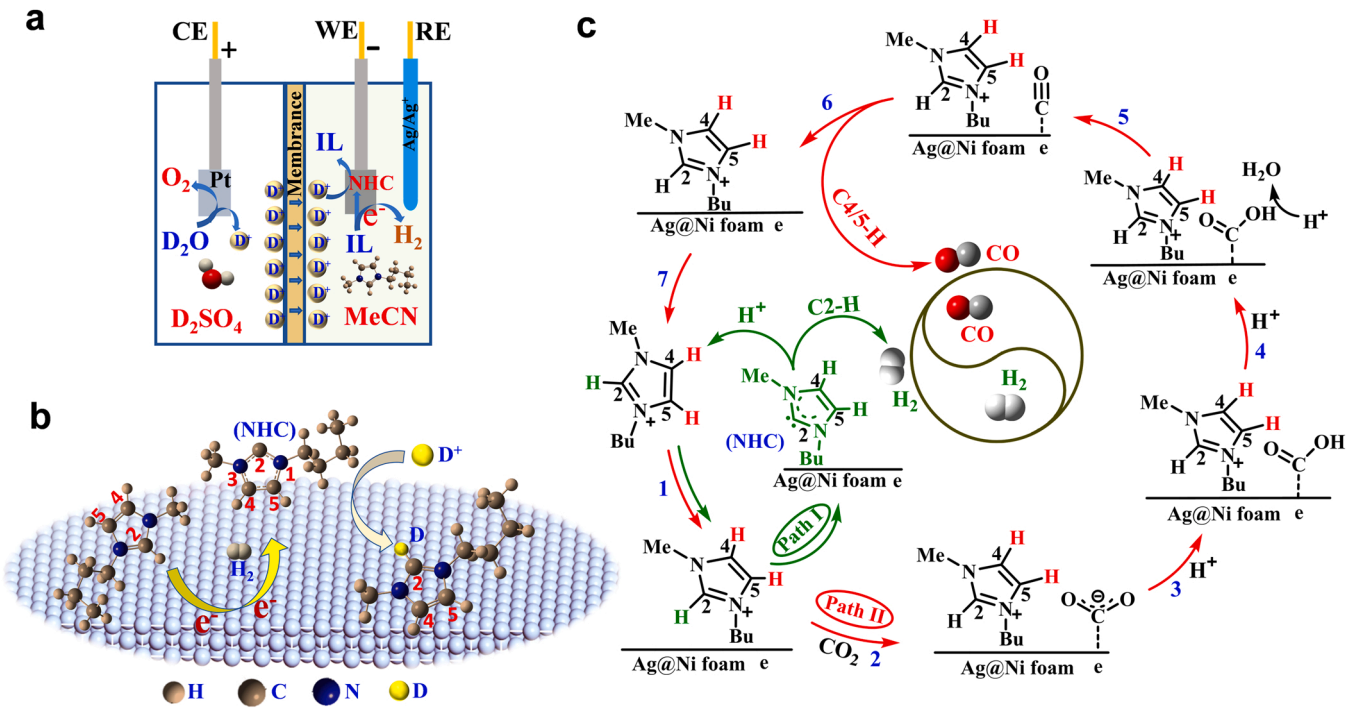

Fig. 6. (a) Schematic of the electrochemical H-cell used for H/D exchange, (b) the H/D exchange process of cationic C2-H under electrochemical action in Ar atmosphere, (c) the proposed mechanism for the electrochemical CO_2RR-to-syngas in [C_4mim][PF_6]/MeCN electrolyte: the green line represents H_2 production predominantly controlled by imidazolium cationic C2-H (**Path I**), while the red line represents CO production mainly promoted by C4/5-H (**Path II**), and the two reaction pathways are competing.

atmosphere. This result indicates that cationic C2-H was easier to activate under electrolysis, [29,51] and C2-H of the $[C_4mim]^+$ adsorbed on the cathode surface was reduced to H_2 in the Ar atmosphere. In other words, in the absence of CO_2 and water in cathode chamber, imidazolium cationic C2-H would serve as a hydrogen source for HER.

The above process could be described as, at − 1.97 ~ − 2.17 V (vs. Fc/Fc^+), the $[C_4mim]^+$ was first adsorbed on the surface of the nano-Ag@Ni foam, and C2-H was reduced to H_2, while the $[C_4mim]^+$ was transformed to *N*-heterocyclic carbene (NHC). When D^+ in the anode compartment of the electrolytic cell enters the cathode compartment through the proton exchange membrane, NHC recombines with D^+ to generate $[C_4mim]^+$ in which C2-H was replaced by C2-D. If the reduction potentials continue to be reduced, C4/5-H would undergo a reaction similar to that of C2-H, and the electrochemical reduction product was H_2/HD/D_2.

However, in the CO_2 atmosphere and [C_4mim][PF_6]/MeCN electrolyte, only C2-H underwent **H/D** exchange under electrolysis at different potentials (Fig. S21). At − 1.97 V (vs. Fc/Fc^+), there was only H_2 in the reduction product, illustrating that the reduction potential of CO_2 was lower than that of C2-H. Therefore, the first reaction on the nano-Ag@Ni foam electrode was the deprotonation of imidazolium cationic C2-H to generate NHC and then proceed to the **H/D** exchange. At − 2.07 V (vs. Fc/Fc^+), CO appeared in the electrochemical reduction products. However, in the case of a continuous decrease in the reduction potential, no **H/D** exchange was still observed for C4/5-H, which means that the reduction potential of CO_2 was higher than that of C4/5-H. Even when the potential was reduced to − 2.77 V (vs. Fc/Fc^+), **H/D** exchange was not observed for C4/5-H. Similarly, there was no **H/D** exchange on imidazolium cationic C4/5-H in [C_4mmim][PF_6]/MeCN electrolyte (Fig. S22). This result suggests that when the reduction potential of CO_2 was reached, CO_2RR-to-CO became the main pathway to compete with HER, thus protecting C4/5-H from electrochemical effects. Furthermore, ^{1}H NMR and FT-IR spectra (Figs. S23 and S24) of the electrolyte after CO_2RR showed no characteristic peaks of NHC and the adduct of NHC and CO_2 (NHC-CO_2), suggesting that the whole CO_2RR process occurred on the nano-Ag@Ni foam electrode but not in the electrolyte. Based on the in-situ Raman and ^{1}H NMR spectrum analysis, we proposed the possible mechanism for the electrochemical CO_2RR-to-syngas in [C_4mim][PF_6]/MeCN electrolyte, as shown in Fig. 6**c**.

For the electrochemical reduction in [C_4mim][PF_6]/MeCN electrolyte, $[C_4mim]^+$ was first adsorbed on the surface of the nano-Ag@Ni foam catalyst. Because the reduction potential of C2-H was higher than that of CO_2RR, the $[C_4mim]^+$ was preferentially reduced to NHC and H_2, and then the NHC received the H^+ permeated from the anode cell to regenerate $[C_4mim]^+$. In this case, the C2-H contributes to HER, and the process corresponds to **Path I**. When the reduction potential of CO_2 was reached, CO_2RR-to-CO (**Path II**) became the main pathway to compete with HER. At this stage, the product was syngas and the molar ratio of CO/H_2 could be tuned by the competition between **Path I** and **Path II**. However, for the electrochemical reduction in [C_4mmim][PF_6]/MeCN electrolyte, where the imidazolium cationic C2-H was replaced by methyl, the C2-CH_3 cannot provide protons to HER, thus HER on the electrode was greatly reduced, and CO_2RR-to-CO became the main reaction. In this case, C4/5-H may play an important role.

To reveal how C4/5-H of the IL promotes CO_2RR-to-CO process, we investigated the interaction of $[C_4mmim]^+$ with radical intermediate $*COO^-$ using density functional theory (DFT, see details in Supporting Information). As shown in Fig. 7, two different configurations of $[C_4mmim]^+$ interacting with $*COO^-$ were optimized separately, in which hydrogen bonds were formed through C4/5-H with the oxygen atoms of $*COO^-$. However, when one $[C_4mmim]^+$ interacts with one $*COO^-$ (Fig. 7**a**), C4-H and C5-H are ready to form hydrogen bonds, respectively, with oxygen atoms of $*COO^-$ with bond lengths of 2.44 Å and 2.00 Å, and the bonding energy between $[C_4mmim]^+$ and $*COO^-$ was calculated to be −11.37 kcal mol^{-1}. When two $[C_4mmim]^+$ cations interact with one $*COO^-$, C4-H and C5-H synergistically interact with the oxygen atoms of $*COO^-$ in the way shown in Fig. 7**b**, leading to the formation of four hydrogen bonds with bond length of 2.44 Å (C4-H…O), 2.11 Å (C5-H…O), 2.49 Å (C4-H…O), and 2.13 Å (C5-H…O). The total binding energy is calculated to be −19.94 kcal mol^{-1}. By

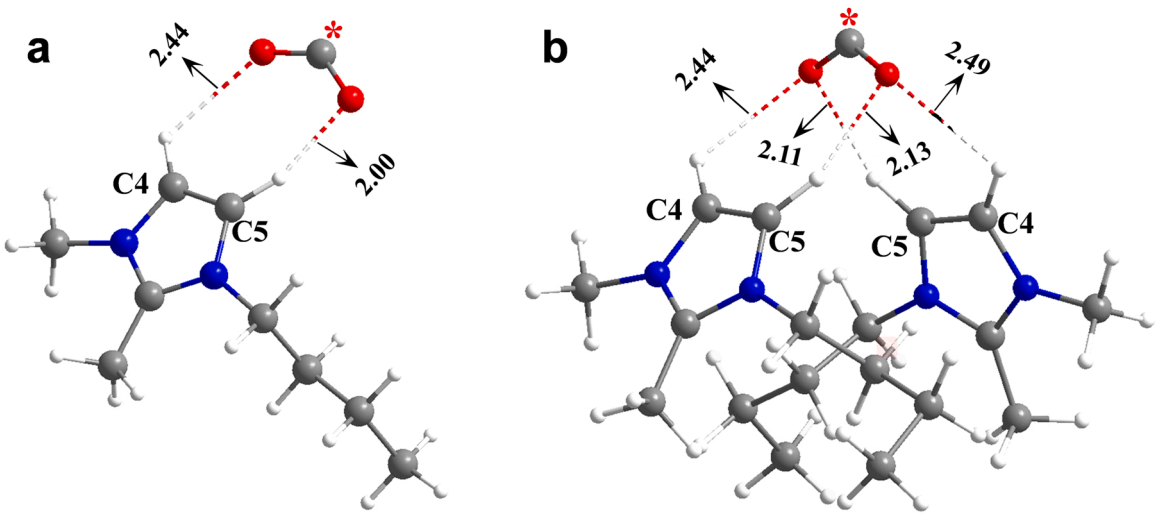

Fig. 7. The binding of *COO$^-$ with one $[C_4mmim]^+$ cation (a) and two $[C_4mmim]^+$ cations (b). The bond length is given in Å.

comparing the binding energy of the two configurations, two $[C_4mmim]^+$ cations are more conducive to the stability of *COO$^-$. This finding is supported by the speculation of Dyson and co-workers [52] that bimolecular $[C_4mmim]^+$ can stabilize the *COO$^-$ radical intermediate through C4-H and C5-H of the IL.

To verify that C4/5-H are the active sites to stabilize radical intermediate *COO$^-$ experimentally, the CO_2RR performance of nano-Ag@Ni foam in 1,2,4,5-tetramethyl-2-ethylimidazolium hexafluorophosphate ([1,2,4,5-MEim][PF_6])/MeCN electrolyte was also investigated, where cationic C2/4/5-H were all replaced by methyl groups. At different reduction potentials, the FE_{CO} values were all lower than 20.4% (Table S5, Fig. S25), which suggests that when C4/5-H was also substituted by methyl groups, the stabilizing effect of the IL on the intermediate was significantly weakened. This indirectly verified that in the imidazolium IL electrolytes, C4/5-H are the active sites to stabilize radical intermediate *COO$^-$. Thus, combined with the results obtained by in-situ Raman spectroscopy, it is clear that the synergistic effect of nano-Ag@Ni foam catalyst and IL electrolyte boosts the superior electrochemical performance of CO_2RR-to-syngas.

4. Conclusions

In summary, we prepared a highly effective nano-Ag@Ni foam catalyst for electrochemical CO_2RR-to-syngas in 30 wt% [C_4mim][PF_6]/MeCN electrolyte. The 3D morphology and excellent contact between the catalyst and the substrate resulted in a large electrochemically active surface area favorable for electrocatalytic CO_2RR to syngas. Importantly, the molar ratio of CO/H_2 in the syngas could be tuned from 1:5–26:1, and the current density was 363.6, 458.2, and 644.7 mA cm^{-2} in a flow cell at the CO/H_2 molar ratio of 1:1, 1:2, and 1:3, respectively. This is comparable to the best result reported so far for electrochemical CO_2RR-to-syngas, and the syngas at these CO/H_2 molar ratios might be directly used for the hydroformylation and Fischer-Tropsch synthesis. Furthermore, we could convert all the CO_2RR products to CO by replacing the C2-H of the imidazolium cation with a methyl group, and the current density was high up to 528.3 mA cm^{-2}. From the combined studies of proton tracer, in-situ Raman, ^{1}H and ^{2}H NMR, and FT-IR spectroscopy, it is revealed for the first time that the reaction intermediates on the nano-Ag@Ni foam catalyst associated with IL electrolytes were *COOH and *CO, whereas in the IL electrolyte, the C2-H of [C_4mim][PF_6] was mainly responsible for H_2 evolution, but the C4/5-H cooperatively stabilized the radical intermediate *COO$^-$ for CO production. Thus, the synergistic effect of nano-Ag@Ni foam catalyst and IL electrolyte remarkably improved the electrocatalytic conversion performance of CO_2RR to syngas. The mechanism proposed here is new for the CO_2RR-to-syngas and the excellent current density is also a step toward industrial applications. In addition, since nano-Ag@Ni foam catalyst is inexpensive, simple in preparation procedure, and easy to scale up, its combination with IL electrolyte is promising for industrial applications of CO_2RR-to-syngas.

CRediT authorship contribution statement

Zhaojun Min and **Jianji Wang** designed the experiments. **Zhaojun Min**, **Maohong Fan**, and **Jianji Wang** wrote the manuscript. **Zhaojun Min**, **Bing Chang**, and **Nan Wang** performed the experiments. **Xiaofang Su** provided quantum chemical calculation support. **Chunfeng Shao**, **Zhiyong Li**, **Huiyong Wang**, and **Yang Zhao** performed the analysis of experimental data. **Jianji Wang** led the project. All authors discussed the results and commented on the manuscript.

Declaration of Competing Interest

The authors declare that they have no known competing financial interests or personal relationships that could have appeared to influence the work reported in this paper.

Data Availability

No data was used for the research described in the article.

Acknowledgments

This work was financially supported by the National Natural Science Foundation of China (No. 22273018, 22233006, and 22273017), and 111 Project (D17007).

Appendix A. Supporting information

Supplementary data associated with this article can be found in the online version at doi:10.1016/j.apcatb.2022.122185.

References

[1] J. Qiao, Y. Liu, F. Hong, J. Zhang Chem. Soc. Rev. 43 (2014) 631–675, https://doi.org/10.1039/c3cs60323g.
[2] M. Zhong, K. Tran, Y.M. Min, C.H. Wang, Z.Y. Wang, C.T. Dinh, P. De Luna, Z. Q. Yu, A.S. Rasouli, P. Brodersen, S. Sun, O. Voznyy, C.S. Tan, M. Askerka, F.L. Che, M. Liu, A. Seifitokaldani, Y.J. Pang, S.C. Lo, A. Ip, Z. Ulissi, E.H. Sargent, Nature 581 (2020) 178–183, https://doi.org/10.1038/s41586-020-2242-8.

[3] G. Cui, J. Wang, S. Zhang, Chem. Soc. Rev. 45 (2016) 4307–4339, https://doi.org/10.1039/C5CS00462D.
[4] D. Zhong, Z. Zhao, Q. Zhao, D. Cheng, B. Liu, G. Zhang, W. Deng, H. Dong, L. Zhang, J. Li, J. Li, J. Gong, Angew. Chem. Int. Ed. 60 (2021) 4879–4885, https://doi.org/10.1002/anie.202015159.
[5] J. Gu, C.S. Hsu, L.C. Bai, H.M. Chen, X.L. Hu, Science 364 (2019) 1091–1094, https://doi.org/10.1126/science.aaw7515.
[6] Z. Zhang, L. Zhao, Z. Xie, Z. Zhou, Green. Chem. Eng. 1 (2020) 79–81, https://doi.org/10.1016/j.gce.2020.10.003.
[7] R. Daiyan, R. Chen, P. Kumar, N.M. Bedford, J. Qu, J.M. Cairney, R. Amal, ACS Appl. Mater. Interfaces 12 (2020) 9307–9315, https://doi.org/10.1021/acsami.9b21216.
[8] M. Zhang, Z. Hu, L. Gu, Q. Zhang, L. Zhang, Q. Song, W. Zhou, S. Hu, Nano Res. 13 (2020) 3206–3211, https://doi.org/10.1007/s12274-020-2988-1.
[9] R. He, A. Zhang, Y. Ding, T. Kong, Q. Xiao, H. Li, Y. Liu, J. Zeng, Adv. Mater. 30 (2018), 1705872, https://doi.org/10.1002/adma.201705872.
[10] Y. Liu, D. Tian, A.N. Biswas, Z. Xie, S. Hwang, J.H. Lee, H. Meng, J.G. Chen, Angew. Chem. Int. Ed. 59 (2020) 11345–11348, https://doi.org/10.1002/anie.202003625.
[11] J. Wu, Y. Xie, Z. Ren, S. Du, H. Meng, L. Zhao, X. Wang, G. Wang, H. Fu, Chemsuschem 12 (2019) 3304–3311, https://doi.org/10.1002/cssc.201901120.
[12] L. Mascaretti, A. Niorettini, B.R. Bricchi, M. Ghidelli, A. Naldoni, S. Caramori, S. Berardi, ACS Appl. Energy Mater. 3 (2020) 4658–4668, https://doi.org/10.1021/acsaem.0c00301.
[13] F. Sastre, M.J. Muñoz-Batista, A. Kubacka, M. Fernández-García, W.A. Smith, F. Kapteijn, M. Makkee, J. Gascon, Chemelectrochem 3 (2016) 1497–1502, https://doi.org/10.1002/celc.201600392.
[14] Z.B. Hoffman, T.S. Gray, K.B. Moraveck, T. Brent Gunnoe, G. Zangari, ACS Catal. 7 (2017) 5381–5390, https://doi.org/10.1021/acscatal.7b01161.
[15] S. Lamaison, D. Wakerley, D. Montero, G. Rousse, D. Taverna, D. Giaume, D. Mercier, J. Blanchard, H.N. Tran, M. Fontecave, M. Mougel, Chemsuschem 12 (2019) 511–517, https://doi.org/10.1002/cssc.201802287.
[16] K. Lv, C. Teng, M. Shi, Y. Yuan, Y. Zhu, J. Wang, Z. Kong, X. Lu, Y. Zhu, Adv. Funct. Mater. 28 (2018), 1802339, https://doi.org/10.1002/adfm.201802339.
[17] R. He, X. Yuan, P. Shao, T. Duan, W. Zhu, Small 15 (2019), 1904882, https://doi.org/10.1002/smll.201904882.
[18] Y.E. Kim, B. Kim, W. Lee, Y.N. Ko, M.H. Youn, S.K. Jeong, J. Oh, Chem. Eng. J. 413 (2021), 127448, https://doi.org/10.1016/j.cej.2020.127448.
[19] Q. He, D. Liu, J.H. Lee, Y. Liu, Z. Xie, S. Hwang, S. Kattel, L. Song, J.G. Chen, Angew. Chem. Int. Ed. 59 (2020) 3033–3037, https://doi.org/10.1002/anie.201912719.
[20] J. Leverett, R. Daiyan, L. Gong, K. Iputera, Z. Tong, J. Qu, R. Amal, ACS nano 15 (2021) 12006–12018, https://doi.org/10.1021/acsnano.1c03293.
[21] B. Chang, X.G. Zhang, Z. Min, W. Lu, Z. Li, J. Qiu, H. Wang, J. Fan, J. Wang, J. Mater. Chem. A 9 (2021) 17876–17884, https://doi.org/10.1039/D1TA03854K.
[22] W. Ni, Z. Liu, X. Guo, Y. Zhang, C. Ma, Y. Deng, S. Zhang, Appl. Catal. B Environ. 291 (2021), 120092, https://doi.org/10.1016/j.apcatb.2021.120092.
[23] N. Meng, C. Liu, Y. Liu, Y. Yu, B. Zhang, Angew. Chem. Int. Ed. 58 (2019) 18908–18912, https://doi.org/10.1002/anie.201913003.
[24] H. Wang, Y. Wu, Y. Zhao, Z. Liu, Acta Phys. Chim. Sin. 37 (2021), 2010022. ⟨http://www.whxb.pku.edu.cn/EN/10.3866/PKU.WHXB202010022⟩.
[25] W.D. Gonçalves, M. Zanatta, N.M. Simon, L.M. Rutzen, D.A. Walsh, J. Dupont, Chemsuschem 12 (2019) 4170–4175, https://doi.org/10.1002/cssc.201901076.
[26] Z. Min, Z. Li, H. Wang, X. Xuan, Y. Zhao, J. Wang, ACS Sustain. Chem. Eng. 9 (2021) 853–862, https://doi.org/10.1021/acssuschemeng.0c07578.
[27] Y. Pei, Y. Zhang, J. Ma, M. Fan, S. Zhang, J. Wang, Mater. Today Nano. 17 (2022), 100159, https://doi.org/10.1016/j.mtnano.2021.100159.
[28] W. Lu, B. Jia, B. Cui, Y. Zhang, K. Yao, Y. Zhao, J. Wang, Angew. Chem. Int. Ed. 56 (2017) 11851–11854, https://doi.org/10.1002/anie.201703977.
[29] A. Kemna, N. García Rey, B. Braunschweig, ACS Catal. 9 (2019) 6284–6292, https://doi.org/10.1021/acscatal.9b01033.
[30] B. Deng, M. Huang, X. Zhao, S. Mou, F. Dong, ACS Catal. 12 (2021) 331–362, https://doi.org/10.1021/acscatal.1c03501.
[31] N. Hollingsworth, S.F. Rebecca Taylor, M.T. Galante, J. Jacquemin, C. Longo, K. B. Holt, N.H. de Leeuw, C. Hardacre, Angew. Chem. Int. Ed. 127 (2015) 14370–14374, https://doi.org/10.1002/ange.201507629.
[32] T. Pardal, S. Messias, M. Sousa, A.S.R. Machado, C.M. Rangel, D. Nunes, M.N. da Ponte, J. CO_2 Util. 18 (2017) 62–72, https://doi.org/10.1016/j.jcou.2017.01.007.
[33] S. Messias, M.M. Sousa, M.N. da Ponte, C.M. Rangel, T. Pardal, A.S.R. Machado, React. Chem. Eng. 4 (2019) 1982–1990, https://doi.org/10.1039/C9RE00271E.
[34] D. Yang, Q. Zhu, X. Sun, C. Chen, W. Guo, G. Yang, B. Han, Angew. Chem. Int. Ed. 132 (2020) 2374–2379, https://doi.org/10.1002/ange.201914831.
[35] S. Back, M.S. Yeom, J. Yung, ACS Catal. 5 (2015) 5089–5096, https://doi.org/10.1021/acscatal.5b00462.
[36] N. Zhang, X. Zhang, L. Tao, P. Jiang, C. Ye, R. Lin, Z. Huang, A. Li, D. Pang, H. Yan, Y. Wang, P. Xu, S. An, Q. Zhang, L. Liu, S. Du, X. Han, D. Wang, Y. Li, Angew. Chem. Int. Ed. 60 (2021) 6170–6176, https://doi.org/10.1002/anie.202014718.
[37] X. Wu, Y. Guo, Z. Sun, F. Xie, D. Guan, J. Dai, F. Yu, Z. Hu, Y.-C. Huang, C.-W. Pao, J.-L. Chen, W. Zhou, Z. Shao, Nat. Commun. 12 (2021) 1–11, https://doi.org/10.1038/s41467-021-20960-8.
[38] K. Sun, Z. Zhang, C. Shen, N. Rui, C. Liu, Green. Energy Environ. (2021), https://doi.org/10.1016/j.gee.2021.05.004. ⟨https://doi.org/10.1016/j.gee.2021.05.004⟩.
[39] S. Dey, S. Podder, A. Roychowdhury, D. Das, C.K. Ghosh, J. Environ. Manag. 211 (2018) 356–366, https://doi.org/10.1016/j.jenvman.2018.01.009.
[40] Y. Zhang, Synth. React. Inorg. M 46 (2016) 1565–1570, https://doi.org/10.1080/15533174.2015.1137027.
[41] C. Liu, F. Wang, D. Jia, J. Zhang, J. Zhang, Q. Hao, J. Zhang, Y. Li, H. Liu, Nanoscale 12 (2020) 19333–19339, https://doi.org/10.1039/D0NR04855K.
[42] B. Eftekharinia, H. Pezeshki, A. Dabirian, ACS Appl. Mater. Interfaces 12 (2020) 17424–17435, https://doi.org/10.1021/acsami.9b22622.
[43] J. Yan, Z. Fan, W. Sun, G. Ning, T. Wei, Q. Zhang, R. Zhang, L. Zhi, F. Wei, Adv. Funct. Mater. 22 (2012) 2632–2641, https://doi.org/10.1002/adfm.201102839.
[44] D.H. Kwon, S.R. Lee, Y.S. Choi, S.B. Son, K.H. Oh, K. Char, M. Kim, Phys. Status Solidi-R. 11 (2017), 1700048, https://doi.org/10.1002/pssr.201700048.
[45] L. Zhuang, L. Ge, Y. Yang, M. Li, Y. Jia, X. Yao, Z. Zhu, Adv. Mater. 29 (2017), 1606793, https://doi.org/10.1002/adma.201606793.
[46] L. Sha, K. Ye, J. Yin, K. Zhu, K. Cheng, J. Yan, G. Wang, D. Cao, Chem. Eng. J. 381 (2020), 122603, https://doi.org/10.1016/j.cej.2019.122603.
[47] W. Gao, S. Emaminejad, H.Y.Y. Nyein, S. Challa, K. Chen, A. Peck, H.M. Fahad, H. Ota, H. Shiraki, D. Kiriya, D.-H. Lien, G.A. Brooks, R.W. Davis, A. Javey, Nature 529 (2016) 509–514, https://doi.org/10.1038/nature16521.
[48] J. Gao, H. Zhang, X. Guo, J. Luo, S.M. Zakeeruddin, D. Ren, M. Grätzel, J. Am. Chem. Soc. 141 (2019) 18704–18714, https://doi.org/10.1021/jacs.9b07415.
[49] W. Shan, R. Liu, H. Zhao, Z. He, Y. Lai, S. Li, J. Liu, ACS Nano 14 (2020) 11363–11372, https://doi.org/10.1021/acsnano.0c03534.
[50] A. Herzog, A. Bergmann, H.S. Jeon, J. Timoshenko, S. Kühl, C. Rettenmaier, B. Roldan Cuenya, Angew. Chem. Int. Ed. 60 (2021) 7426–7435, https://doi.org/10.1002/anie.202017070.
[51] S. Neyrizi, J. Kiewiet, M.A. Hempenius, G. Mul, ACS Energy Lett. 7 (2022) 3439–3446, https://doi.org/10.1021/acsenergylett.2c01372.
[52] G.P. Lau, M. Schreier, D. Vasilyev, R. Scopelliti, M. Grätzel, P.J. Dyson, J. Am. Chem. Soc. 138 (2016) 7820–7823, https://doi.org/10.1021/jacs.6b03366.